Chinese Chemical Letters 32 (2021) 2837–2840

Contents lists available at ScienceDirect

Chinese Chemical Letters

journal homepage: www.elsevier.com/locate/cclet

Communication

Engineering $BiOBr_xI_{1-x}$ solid solutions with enhanced singlet oxygen production for photocatalytic benzylic C—H bond activation mediated by *N*-hydroxyl compounds

Yucui Bian, Yongpan Gu, Xiaofei Zhang, Haijun Chen*, Zhongjun Li*

Green Catalysis Center, College of Chemistry, Zhengzhou University, Zhengzhou 450001, China

ARTICLE INFO

Article history:
Received 9 December 2020
Received in revised form 25 December 2020
Accepted 1 February 2021
Available online 4 February 2021

Keywords:
$BiOBr_xI_{1-x}$ solid solutions
Ethylbenzene oxidation
N-Hydroxysuccinimide
Photocatalysis
Singlet oxygen

ABSTRACT

The aerobic, selective oxidation of hydrocarbons *via* C—H bond activation is still a challenge. This work shows the achievement of the room temperature visible light driven photocatalytic activation of benzylic C—H bonds with *N*-hydroxysuccinimide over $BiOBr_xI_{1-x}$ ($0 \le x \le 1$) solid solutions, whose valance bands were engineered through varying the ratio of bromide to iodide. The optimal $BiOBr_{0.85}I_{0.15}$ catalyst exhibited over 98% conversion ratio of ethylbenzene, which was about 3.9 and 8.9 times that of pure BiOBr and BiOI, respectively. The excellent photocatalytic activity of $BiOBr_{0.85}I_{0.15}$ solid solution can be ascribed to the orbital hybridization of the valence band containing both Br 4p and I 5p orbitals, which could promote photo-induced charge carrier separation and improve the generation of singlet oxygen. This work shed some light on the rational design of photocatalysts for targeted organic transformation.

Selective functionalization of benzylic $C(sp^3)$ C—H bonds of hydrocarbons with molecular oxygen (O_2) plays a very important role in pharmaceuticals and fine chemicals synthesis [1,2]. However, due to the huge resonance stabilization energy in ground triplet state $^3\Sigma_g^-O_2$, it is thermodynamically unfavorable for O_2 to directly interact with organic molecules [3]. Photocatalysts are usually employed to activate O_2 into various reactive oxygen species [4]. Especially, the singlet oxygen $^1O_2$, which is an active species with relatively mild oxidizing ability toward high selectivity and generally associated with the synthesis of natural products and drugs [4,5], is beneficial to selectively activating the C—H bonds to form oxygenated products.

The direct selective activation of $C(sp^3)$—H bonds has attracted enormous attentions [6], to which great efforts have been devoted including the use of transition metal complexes as homogeneous catalysts and the heterogeneous catalysis with rather stringent reaction conditions, such as high temperature and pressure [7,8], while it is still a hot topic to selectively oxidize these inert bonds under mild conditions due to the high bond dissociation energy of $C(sp^3)$—H bonds (70–130 kcal/mol) [9–11]. Alternatively, the C—H bonds can readily react with *N*-oxyl radicals to form carbon radicals *via* H-abstraction [12,13], which is an efficient route to achieve the hydrocarbon oxidation under mild conditions. However, the production of *N*-oxyl radicals, which is firstly induced from *N*-hydroxy compounds, still requires radical initiators such as azo compounds, metal salts, NO_x, or quinone [14–16]. To tackle this issue, heterogeneous photocatalysis is deemed as one of the most promising way to generate the *N*-oxyl radicals with energy renewable, environmentally friendly merits, which follows in the scope of the sustainable chemistry. Whereas, up to now, only a few specific visible light-responsive catalysts, such as C_3N_4, CdS, and FeO_x, could produce efficient *N*-oxyl radicals through oxidation of *N*-hydroxyphthalimide by photogenerated holes [17–20]. Therefore, it would be significant and highly desirable to explore other efficient photocatalytic system to regulate *N*-oxyl radicals generation for activating C—H bonds.

Solid solution materials have been intensively investigated in photocatalysis field due to their flexible and effective modulation of the energy band structures [21,22]. Among them, bismuth oxyhalide solid solution, as a new type of two dimensional material with open layered structure possessing attractive physicochemical properties, for example, internal electric field [23], low toxicity, adjustable optical absorptions, and enhanced charge separation, was extensively used for photocatalytic degradation of organic pollutants [24], reduction of CO_2 [25], and elimination of NO [26]. Moreover, the regulation of band structure of solid solution could also adjust the activation capacity of reactive oxygen species.

---

* Corresponding authors.
E-mail addresses: chenhaijun@zzu.edu.cn (H. Chen), lizhongjun@zzu.edu.cn (Z. Li).

https://doi.org/10.1016/j.cclet.2021.02.006

Inspired by the above investigations, we intended to engineer solid solution to achieve selective benzylic C—H bond activation through regulating specific reactive oxygen species production involved by succinimide-*N*-oxyl radicals (SINO). Herein, the $BiOBr_xI_{1-x}$ solid solutions with adjustable band structure and redox potentials were used to study their photocatalytic performance for aerobic oxidation of C(sp^3)—H bonds to corresponding oxygenated products at room temperature with the assistance of *N*-hydroxysuccinimide (NHSI). The possible mechanism of synergistic effect of enhanced carrier separation and singlet oxygen production by solid solution toward improved photocatalytic performance was revealed.

The crystal phase purity of the as-prepared $BiOBr_xI_{1-x}$ solid solutions (denoted as BBI-*x*, $0 \le x \le 1$, hereafter) was identified by X-ray diffraction (XRD) measurements in Fig. 1a. The diffraction peaks of the pure BiOBr (BB) and BiOI (BI), which are in keeping with the standard XRD patterns of BiOBr (JCPDS No. 09-0393) and BiOI (JCPDS No. 10-0445) in the tetragonal phase, respectively, demonstrating the tetragonal structure of the BBI-*x*. When the value of *x* decreased, the peaks of BBI-*x* presented a slight shift toward lower 2θ angles, which was arising from the replacement of bromide ions by iodide ions with a larger radius (Br: 1.95 Å *vs.* I: 2.16 Å). In addition, the changes in the lattice parameters of the solid solution further confirm that iodide ions were successfully incorporated into the BB lattice, and the interplanar lattice spacing of BBI-*x* was calculated by the Bragg's law in Table S1 (Supporting information) [27,28]. The lattice parameter *c* exhibited a nearly linear relationship with the Br mole fraction (Fig. 1b). Notably, the calculated value of *c* deviated from Vegard’s law, which may be mainly due to the weakness of anion-anion interactions across the interface between two adjacent halide anion layers [28]. These regular movements in XRD peaks position and the variation of the *c* indicate that the obtained catalysts are solid solutions rather than a mixture of BB and BI [24].

The morphology and microstructure of the as-synthesized BBI-*x* catalysts were examined by scanning electron microscope (SEM), N_2 adsorption, and transmission electron microscope (TEM). As depicted by Fig. 2a, when none of iodide ion was doped, the obtained BB catalyst exhibited a bent sheet-like two-dimensional morphology, which still presented in BBI-0.85 ($BiOBr_{0.85}I_{0.15}$) catalyst when 15% molar ratio of bromine was replaced by iodine, while BBI-0.6 ($BiOBr_{0.6}I_{0.4}$), BBI-0.4 ($BiOBr_{0.4}I_{0.6}$), BBI-0.2 ($BiOBr_{0.2}I_{0.8}$), and BI catalysts showed spherical structure assembled by the nanosheet, as illustrated in Fig. S1 (Supporting information) and Figs. 2b and c. These results demonstrate that the content of iodine has a remarkable effect on the assembly mode of the solid solution. Table S2 and Fig. S2 (Supporting information) showed that the surface areas of BB, BBI-0.85, and BI were calculated to be 6.04 m^2/g, 22.40 m^2/g, and 29.21 m^2/g, respectively. Further, the TEM images in Figs. 2d–f clearly showed the similar nanosheet structure of BB, BBI-0.85, and BI, which were in line with the SEM images. The high-resolution TEM (HRTEM) images revealed the high degree of crystallinity and the clear lattice fringes of catalysts in Figs. 2g–i. For BBI-0.85 solid solution, the d-spacing of 0.280 nm were coincided with the (110) plane of the tetragonal structure (Fig. 2h). Moreover, the interplanar lattice spacing value of BBI-0.85 falls in between that of 0.278 nm of pure BB and 0.285 nm of BI (Figs. 2g and i), which further confirms the formation of solid solution containing mixed halides. And the energy-dispersive X-ray spectrometer mapping images showed that the Bi, O, Br, and I elements were evenly distributed in BBI-0.85 nanosheet in Fig. S3 (Supporting information).

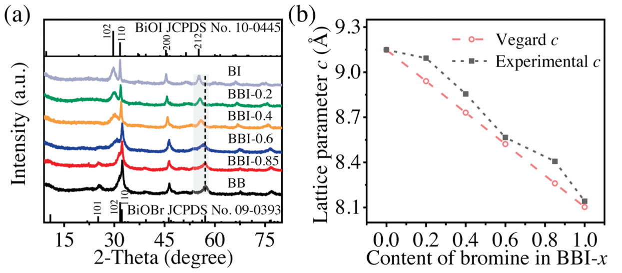

Fig. 1. (a) X-ray diffraction patterns of BBI-*x* catalysts. (b) Variation of the lattice parameter *c* of the BBI-*x* solid solutions with Br mole fraction.

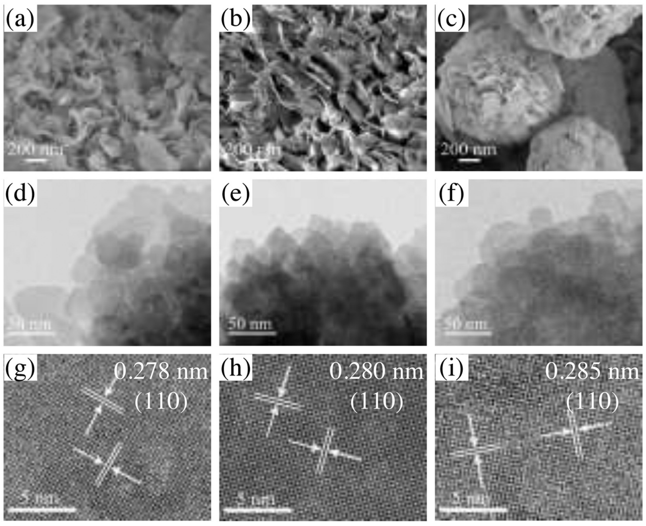

Fig. 2. SEM, TEM, and HRTEM images of BB (a, d, g), BBI-0.85 (b, e, h), and BI (c, f, i) catalysts, respectively.

The UV–vis diffuse reflectance spectra analysis was adopted to characterize the optical properties of BBI-*x* solid solutions (Fig. S4a in Supporting information). With the increasing of the content of iodine, the optical absorption edges of the BBI-*x* catalysts underwent a red shift from 440 nm of BB to 664 nm of BI. The energy band gap (E_g) of BBI-*x* (*x* = 0, 0.2, 0.4, 0.6, 0.85, and 1.0) were calculated to be 1.68, 1.75, 1.80, 1.96, 2.17, and 2.59 eV (Fig. S4b in Supporting information), respectively. Besides, the conduction band (CB) of BBI-*x* solid solutions can be determined by Mott–Schottky measurements (Fig. S4c in Supporting information) [29], and the valence band (VB) edges of catalysts could be obtained by the formula of $E_{VB} = E_g - E_{CB}$, which were found to be 1.40, 1.46, 1.57, 1.75, 1.93, and 2.38 V *vs.* NHE for BI, BBI-0.2, BBI-0.4, BBI-0.6, BBI-0.85, and BB, respectively (Fig. S4d in Supporting information). It has been revealed by density functional theory calculations that the CB of BBI-*x* was mainly composed of Bi 6p orbitals while the VB was consist of Bi 6s, O 2p, Br 4p, and I 5p orbitals and the doping of iodine into BB gave rise to upshift of the VB potential due to the hybridization of Br and I np orbitals, which resulted in the electrons being photo-excited more easily [24]. Accordingly, the light absorption was broadened and the band structures regulated through the solid solution engineering.

The aerobic visible light photo-oxidation of ethylbenzene was selected as a model reaction in Scheme 1 to assess the photocatalytic performance of the solid solutions. As shown in Fig. 3a, NHSI or BBI-0.85 solid solution alone could not oxidize

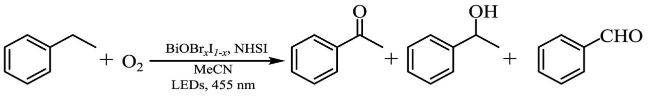

Scheme 1. Aerobic oxidation of ethylbenzene.

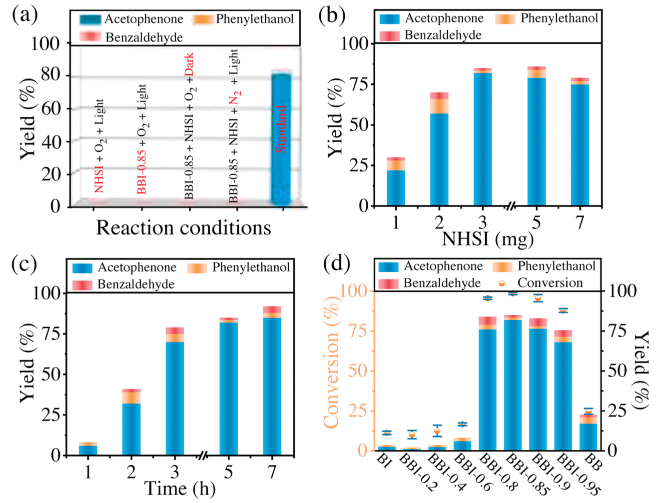

Fig. 3. (a) Photocatalytic oxidation of ethylbenzene over different reaction conditions. (b) Dependences of oxidation products yield on the NHSI concentration in the ethylbenzene oxidation over BBI-0.85 catalyst. (c) Time-dependence of oxidation products yield over BBI-0.85. (d) Photocatalytic oxidation of ethylbenzene over diverse catalysts. Conditions: 10 mg of catalyst, 0.1 mmol of ethylbenzene, 3 mg of NHSI, 3.0 mL of CH_3CN, O_2 at 1 atm, room temperature, blue LED light (455 nm, 8 W), 5 h.

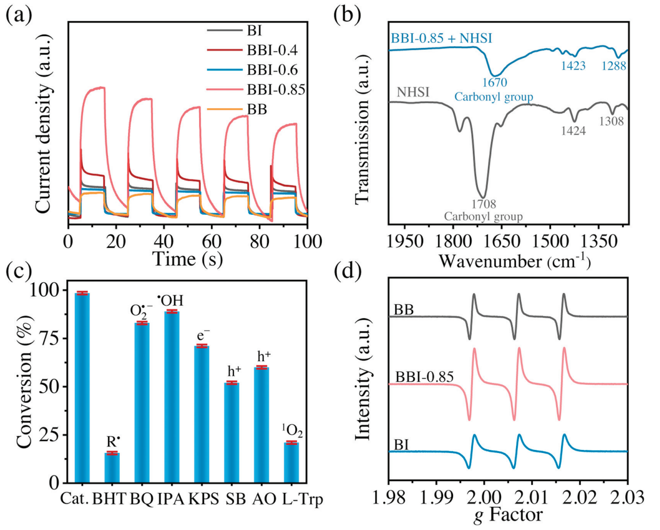

Fig. 4. (a) Photocurrent-time curves. (b) FT-IR spectra of NHSI and adsorbed NHSI on BBI-0.85 catalyst. (c) Ethylbenzene conversions over BBI-0.85 catalyst with different scavengers. (d) EPR spectra of $^1O_2$ over different catalysts in the presence of TEMP.

ethylbenzene under photoirradiation in the presence of O_2. A combination of BBI-0.85 and NHSI can catalyze ethylbenzene with 98% conversion in atmospheric O_2 under 455 nm irradiation. Nevertheless, almost no conversion occurred in the mixture of NHSI and BBI-0.85 photocatalyst in the dark or in the absence of O_2. These experiments clearly demonstrate that BBI-0.85, NHSI, and O_2 were essential to the process of photocatalytic C—H bond activation. Fig. 3b exhibited that the ethylbenzene conversion initially increased with the amounts of NHSI arising, when the quantity of NHSI reached to 3 mg, the conversion reached a plateau. As shown in Fig. 3c, the total amounts of oxidized products increased sharply in three hours, and the intermediate product phenylethanol was further oxidized to acetophenone with increasing irradiation time.

To investigate the relationship between the catalytic performances and the variation of iodide concentration, the photocatalytic activity of a range of BBI-*x* catalysts (*x* = 0, 0.2, 0.4, 0.6, 0.8, 0.85, 0.9, 0.95, 1) were investigated. As shown in Fig. 3d, the catalytic activity initially increased and then decreased with the increasing of the content of iodide, and BBI-0.85 photocatalyst exhibited the highest conversion rate with 98%, which was about 3.9 and 8.9 times that of BB and BI catalysts, respectively. The apparent quantum efficiency (AQE) can reach 0.72% at 445 nm over BBI-0.85 catalyst. These results indicate that the construction of solid solution can significantly improve the photocatalytic activity.

To explore the origin of the excellent photoactivity of solid solutions, we evaluated the photogenerated electron holes separation efficiency of these catalysts by (photo)electrochemical measurements. Photocurrent-time curves of BBI-0.85 exhibited a higher photocurrent density in contrast to the other four catalysts (BI, BBI-0.4, BBI-0.6, and BB) in Fig. 4a. And Fig. S5 (Supporting information) showed that the diameter of the arc radius of BBI-0.85 was clearly much smaller than the other four photocatalysts in electrochemical impedance spectroscopy measurements. The time-resolved photoluminescence spectra was further applied to uncover the detailed information with respect to the carrier kinetics of the solid solutions (Fig. S6 in Supporting information). It can be seen that the calculated average lifetime of the carriers ($\tau_{avg} = (A_1\tau_1^2 + A_2\tau_2^2)/(A_1\tau_1 + A_2\tau_2)$) were 7.07 μs for the BBI-0.85, which was longer than that of BI (6.12 μs), BBI-0.2 (6.58 μs), BBI-0.4 (6.37 μs), BBI-0.6 (6.29 μs), and BB (6.18 μs), respectively (Table S3 in Supporting information). The longer charge carrier lifetime of solid solutions than that of the monocomponent ones indicates that the hybridization of the halogen orbitals in the valence band contributes to prolonging the lifetime of the photogenerated charge and the BBI-0.85 catalyst has the best photoinduced charge separation efficiency. Due to the hybridization of different halogen np orbitals of solid solutions, the mobility of photon-induced holes is decreased, whereas electron mobility is not affected [24,30]. Consequently, the BBI-*x* solid solution displayed considerably reduced recombination efficiency of photogenerated electron holes and enhanced photocatalytic performances.

The oxidation potential of the semiconductor is a key factor that drives the chemical transformation, the more positive of the VB potential, the higher oxidation ability of the photocatalyst. A volcano relationship was obtained between VB potential and photocatalytic performance of BBI-*x* solid solutions in Fig. S7 (Supporting information). Notably the redox potential of NHSI/SINO was determined to be 1.1 V *vs*. NHE by the cyclic voltammetry in Fig. S8 (Supporting information). Therefore, the VB potential in the range of 1.40–2.38 V of the BBI-*x* solid solutions could all be capable of oxidizing NHSI to produce SINO radical, which was the initially reactive species for C—H bond activation [17,18]. In addition, the strong interaction between NHSI and BBI-0.85 surface was clearly demonstrated by Fourier transform infrared spectroscopy (FT-IR) tests (Fig. 4b). The clear red-shift of C=O vibration to 1670 cm^{-1} of BBI-0.85 mixing with NHSI, compared with free NHSI at 1708 cm^{-1}, signifies the adsorption of NHSI on BBI-0.85 surface, which would facilitate the charge transfer [17]. Although, the oxidation of NHSI to SINO radical could be smoothly proceeded over all the solid solutions, the highest oxidation activity for ethylbenzene over BBI-0.85 indicates the electron holes separation was the rate determining step taking (photo)electrochemical results into account.

Further, to get insights into the main reactive species during the photocatalytic process, we carried out a series of radical trapping experiments as shown in Fig. 4c. Adding 2,6-ditert-butyl-4-methylphenol (BHT) can almost inhibit the reaction completely, indicating a carbon-centered radical was involved, which was firstly generated by the trigger of SINO radicals [17]. When

$O_2^{\bullet-}$ capture reagent of 1, 4-benzoquinone (BQ) and $^{\bullet}OH$ capture reagent of isopropanol (IPA) were added separately [31], we obtained a slight decrease in ethylbenzene conversion, indicating that $O_2^{\bullet-}$ and $^{\bullet}OH$ were not key intermediates in the reaction. As electron capture reagents of $K_2S_2O_8$ (KPS) as well as hole capture reagents of $(NH_4)_2C_2O_4$ (AO) and $NaHCO_3$ (SB) were added [32], the ethylbenzene conversion were reduced from 98% to 71%, 62%, and 50%, respectively, verifying the more important role of hole. Notably, the hole would directly oxidize the NHSI to produce SINO radical and then promote the cleavage of C—H bonds [17,19]. The moderate inhibition role of hole scavenger suggests the SINO radical may also be generated by the other way.

It is noteworthy that the L-tryptophan (L-Trp) can dramatically suppress the conversion of ethylbenzene, proving that singlet oxygen plays a vital role in the oxidation reaction (Fig. 4c). Additionally, electron paramagnetic resonance (EPR) measurements were performed with 2,2,6,6-tetramethylpiperidine (TEMP) as a trapping agent. As shown in Fig. 4d, a 1:1:1 triplet signal with *g*-value of 2.006 appeared in the presence of BBI-0.85 under photoirradiation, in accordance with TEMP-$^1O_2$ [33,34]. The higher singlet oxygen signal intensity over BBI-0.85 nanosheets than those of BB and BI catalysts indicated the prominent production of singlet oxygen. Considering that the reaction can hardly occur without NHSI and the oxidation of NHSI to SINO radical was the initial step in ethylbenzene oxidation, which was traditionally considered to be triggered by holes generated in photocatalyst. While the SINO radical still existed to promote the photo-oxidation of ethylbenzene as evidenced by the hole capture experiments. Therefore, we conclude that besides the oxidation of holes, the $^1O_2$ would also oxidize NHSI to produce SINO radical with H_2O_2 as the by-product, which was supported by the ultraviolet visible spectroscopy detective experiments in Fig. S9 (Supporting information).

In view of the above experimental and characteristic results, a plausible reaction pathway for ethylbenzene photooxidation by BBI-*x*/NHSI (>N—OH) was illustrated in Scheme S1 (Supporting information). Under visible light irradiation, photo-induced electron holes are generated. The photosensitized processes would transfer energy to the triplet state oxygen molecules, which results in the generation of $^1O_2$. The photogenerated holes in the VB and $^1O_2$ can directly oxidize >N—OH to form >N—O$^{\bullet}$ (SINO) radicals and H_2O_2 species. Then, the *N*-oxyl radicals can abstract the H$^{\bullet}$ of the C—H bond to form 1-phenethyl carbon radical ($PhCH^{\bullet}CH_3$) intermediates. Meanwhile, the >N—O$^{\bullet}$ radical is reduced to >N—OH for the next run. The $PhCH^{\bullet}CH_3$ radical reacts with activated oxygen to form the phenylethyl peroxide radical ($PhCH(OO^{\bullet})CH_3$), which finally decomposed into the corresponding alcohol and ketone. And the alcohol would also be oxidized to ketone. In addition, C—C bonds may be cleaved by phenylethyl hydrogen peroxide ($PhCH(OOH)CH_3$) compound to give benzaldehyde and CO_2 as the by-products, the latter was determined by gas chromatograph.

In conclusion, BBI-*x* solid solution photocatalysts has been successfully constructed for the selective photocatalytic oxidation of C(sp^3)—H bonds under mild conditions. The $BiOBr_{0.85}I_{0.15}$ solid solution showed an enhanced photocatalytic activity with promoted charge separation efficiency and enhanced generation of singlet oxygen. This study exposes that a rational regulation of solid solution photocatalysts can modulate the activation of oxygen in more challenging organic transformation reactions.

Declaration of competing interest

The authors declare no conflict of interest.

Acknowledgments

This work was supported by the National Natural Science Foundation of China (No. 21671176) and Post-doctoral Foundation of Henan Province.

Appendix A. Supplementary data

Supplementary material related to this article can be found, in the online version, at doi:https://doi.org/10.1016/j.cclet.2021.02.006.

References

[1] H. Sterckx, B. Morel, B.U.W. Maes, Angew. Chem. Int. Ed. 58 (2019) 7946–7970.
[2] K.C. Hwang, A. Sagadevan, Science 346 (2014) 1495–1498.
[3] W.T. Borden, R. Hoffmann, T. Stuyver, B. Chen, J. Am. Chem. Soc. 139 (2017) 9010–9018.
[4] L. Chen, J. Tang, L.N. Song, et al., Appl. Catal. B: Environ. 242 (2019) 379–388.
[5] A.A. Ghogare, A. Greer, Chem. Rev. 116 (2016) 9994–10034.
[6] X.M. Xu, D.M. Chen, Z.L. Wang, Chin. Chem. Lett. 31 (2020) 49–57.
[7] A.E. Shilov, G.B. Shul'pin, Chem. Rev. 97 (1997) 2879–2932.
[8] D. Balcells, E. Clot, O. Eisenstein, Chem. Rev. 110 (2010) 749–823.
[9] X. Cao, Z. Chen, R. Lin, et al., Nat. Catal. 1 (2018) 704–710.
[10] Y. Dai, C. Poidevin, C. Ochoa-Hernández, et al., Angew. Chem. Int. Ed. 59 (2020) 5788–5796.
[11] D.F. McMillen, D.M. Golden, Annu. Rev. Phys. Chem. 33 (1982) 493–532.
[12] Y. Ishii, S. Sakaguchi, T. Iwahama, Adv. Synth. Catal. 343 (2001) 393–427.
[13] Y. Yan, P. Feng, Q.Z. Zheng, et al., Angew. Chem. Int. Ed. 52 (2013) 5827–5831.
[14] M.R. Patil, N.P. Dedhia, A.R. Kapdi, A.V. Kumar, J. Org. Chem. 83 (2018) 4477–4490.
[15] C. Zhang, H. Li, J. Lu, et al., ACS Catal. 7 (2017) 3419–3429.
[16] F. Recupero, C. Punta, Chem. Rev. 107 (2007) 3800–3842.
[17] C. Zhang, Z. Huang, J. Lu, et al., J. Am. Chem. Soc. 140 (2018) 2032–2035.
[18] R. Ma, W. Chen, L. Wang, et al., ACS Catal. 9 (2019) 10448–10453.
[19] G. Zhao, B. Hu, G.W. Busser, et al., ChemSusChem 12 (2019) 2795–2801.
[20] P. Zhang, Y. Wang, J. Yao, et al., Adv. Synth. Catal. 353 (2011) 1447–1451.
[21] J. Li, Y. Yu, L. Zhang, Nanoscale 6 (2014) 8473–8488.
[22] J. Li, W. Yang, A. Wu, et al., ACS Appl. Mater. Interfaces 12 (2020) 8583–8591.
[23] J. Li, L. Cai, J. Shang, et al., Adv. Mater. 28 (2016) 4059–4064.
[24] Q. Wang, Z. Liu, D. Liu, et al., Appl. Catal. B: Environ. 236 (2018) 222–232.
[25] M. Gao, J. Yang, T. Sun, et al., Appl. Catal. B: Environ. 243 (2019) 734–740.
[26] T. Wu, X. Li, D. Zhang, et al., J. Alloys. Compd. 671 (2016) 318–327.
[27] L. Kong, J. Guo, J.W. Makepeace, et al., Catal. Today 335 (2019) 477–484.
[28] E. Keller, V. Kramer, Z. Naturforsch. B 60 (2005) 1255–1263.
[29] H. Chen, L. Peng, Y. Bian, et al., Appl. Catal. B: Environ. 284 (2021) 119704.
[30] H. Zhang, L. Liu, Z. Zhou, Phys. Chem. Chem. Phys. 14 (2012) 1286–1292.
[31] J. Chen, J. Zhan, Y. Zhang, Y. Tang, Chin. Chem. Lett. 30 (2019) 735–738.
[32] L. Peng, Y. Bian, X. Shen, et al., Chin. Chem. Lett. 31 (2020) 2871–2875.
[33] H. Wang, S. Chen, D. Yong, et al., J. Am. Chem. Soc. 139 (2017) 4737–4742.
[34] B. Shen, C. Dong, J. Ji, et al., Chin. Chem. Lett. 30 (2019) 2205–2210.